J. Wind Eng. Ind. Aerodyn. 145 (2015) 339–350

Contents lists available at ScienceDirect

Journal of Wind Engineering and Industrial Aerodynamics

journal homepage: www.elsevier.com/locate/jweia

Numerical analysis of periodic open-loop flow control on bluff bodies in ground proximity

D. Parkin *, J. Sheridan, M.C. Thompson

Fluids Laboratory for Aeronautical and Industrial Research (FLAIR), Department of Mechanical and Aerospace Engineering, Monash University, Clayton 3800, Australia

ARTICLE INFO

Keywords:
Aerodynamics
Road vehicles
Numerical simulation
Large eddy simulation
Flow control
Drag reduction

ABSTRACT

The effectiveness of open-loop actuation at the rear of near-ground bluff bodies in achieving drag reduction is explored numerically. The investigations are conducted on an infinite-width two-dimensional flat-back Ahmed body of height H, placed at a height of $0.2H$ above ground, using large eddy simulations at a Reynolds number of 23,000. This case better mimics the upper and lower shear layers that might be seen behind a heavy vehicle than previous away-from-ground tests, which have shown significant drag reduction is achievable through the attenuation of von Kármán shedding in the near wake. In this study, this effect is shown to essentially vanish once the body is moved close to a moving ground-plane, because the regular formation of strong compact wake vortices in the near wake is prevented. This is also shown to be the case under natural conditions, where a lower drag coefficient than the away-from-ground case is observed. This is interpreted as the result of a mismatch in wake vorticity shed in the upper and lower shear layers, and the disrupting presence of an extra layer of vorticity at the ground, which act together to limit or even suppress vortex shedding into the wake. The periodic actuation strategy, which attempts to control the separating shear layers and, in turn, the formation and shedding of wake vortices, therefore loses applicability. It is postulated that the open-loop strategy may still be effective if employed on the side rear-edges of a heavy vehicle, even though the upper and lower rear-edges are unlikely to yield much success.

1. Introduction

While rear-edge periodic open-loop flow control has proved successful both experimentally (Pastoor et al., 2008) and numerically (Krajnovic and Fernandes, 2011; Parkin et al., 2014) in reducing the mean drag coefficient $\overline{C}_D$ on bluff bodies in simplified, low Reynolds numbers tests, little research has yet been conducted on its effectiveness in the presence of a ground plane.

The control mechanism targets the natural wake instability, characterised by von Kármán vortex shedding at a non-dimensional frequency known as the Strouhal number $St = fH/U_\infty$ (with f the shedding frequency, H the height of the body and U_∞ the blockage-corrected freestream velocity), and an asymmetrical wake. Through periodic actuation at the rear edges—where the velocity of blowing/sucking is sinusoidal (positive indicates blowing and negative sucking)—the alternating rollup and shedding of the upper and lower shear layers is impeded by the control, which preferentially forces synchronous shedding of wake vortices. This disrupts the natural oscillatory instability, where the induced velocity in the near-wake region due to a newly shed vortex normally contributes to the rollup and development of the next vortex from the opposite shear layer. Instead, with synchronous shedding cross-annihilation between vortices is promoted, leading to less coherent wake vortices which form further from the body, and thus a higher pressure in the wake. This leads to less suction on the base of the body, with a higher mean base pressure coefficient $\overline{C}_{pb}$ and therefore lower $\overline{C}_D$. Indeed, Pastoor et al. (2008) experimentally and Parkin et al. (2014) numerically found optimum actuation frequencies of $St_{act} = 0.15$ and $St_{act} = 0.11$, respectively, notably significantly lower than the natural vortex shedding frequency $St \approx 0.23$.

In this paper, the wake flow generated when the body is placed close to the ground, which is more representative of the upper and lower shear layers behind a heavy vehicle, is analysed with actuation applied at various frequencies, $St_{act} = f_{act} H/U_\infty$ (where f_{act} is the actuation frequency). The results are compared with those without actuation. In addition, the results are also compared with those of Parkin et al. (2014), run under otherwise identical conditions but without the ground plane, allowing for identification of clear differences between the ground proximity and away-from-ground cases.

* Corresponding author.
E-mail address: dparkin7@gmail.com (D. Parkin).

http://dx.doi.org/10.1016/j.jweia.2015.03.016
0167-6105/

The ground effect for bluff body flows, and in particular on the wakes of these flows, is not as well understood. This is unlike the situation for attached flows, such as observed on aircraft or racing-car wings. A more detailed characterisation of the transient wake structure behind 3D bluff bodies at different heights is only now emerging, with the 3D Ahmed body (Ahmed and Ramm, 1984) receiving most attention. There appears to be even less literature on the effect of ground proximity on 2D cylindrical bluff bodies, but Kim and Geropp (1998) provide a sound starting point. For a variety of shapes at $Re_D = 2.2 \times 10^4 - 1.3 \times 10^5$, they found a larger pressure difference between the upper and lower surfaces with decreasing ground clearance—akin to the well-known "cushion" effect that occurs for wing flows. They also observed a lower drag and longer wake for decreasing ground clearance and showed that ground proximity dampens periodic flow behind the body. This makes sense as the two shear-layers are no longer equal, which hinders the global instability mechanism. The reported accompanying decrease in Strouhal number is also expected as the vortex shedding mechanism is weakened.

That study also highlights the importance of a moving ground plane. A moving ground plane is often used in automotive wind-tunnel testing to neutralise the ground boundary layer that would otherwise develop. (In the real world, of course, the ground is stationary and without wind there is no boundary layer.) Unfortunately, this involves expensive infrastructure and is not always possible. Kim and Geropp's research shows substantial differences between moving and non-moving cases in the body pressure distribution, with the non-moving ground exaggerating the pressure differences between lower-front and lower-rear. They also show that for a car-like shape, the lift is higher for a non-moving ground, especially at higher Reynolds numbers, while drag is relatively unchanged. Finally, the non-moving ground significantly shortens the"dead-water" region in the wake, where the fluid recirculates after detachment from the rear-edges of the body, and moves its centre closer to the ground. Krajnovic and Davidson (2005) showed that many of these findings, such as higher lift values and exaggerated pressure differences, persist for 3D objects with a non-moving ground plane. They also found a slight increase in drag, and a more scattered Power Spectral Density (PSD) for both the lift and drag signals, suggesting a non-moving ground interferes with the vortex shedding process in the wake.

Many recent studies explore the ground effect on wakes behind 3D objects, such as the Ahmed body, revealing a highly complex flow structure (Grandemange et al., 2013). It is believed that a more thorough understanding of the infinite-width 2D case, where only an upper and lower shear layer are present, will benefit our understanding of the more complicated structure behind 3D bodies. This study is aimed at filling this gap. The difference between upper and lower shear layer development and the effect this has on the von Kármán instability are key areas of interest. Better understanding here will also help to develop open-loop control systems for bluff bodies in ground proximity, which is also explored here directly through the application of rear-edge periodic actuation.

2. Problem description and methodology

The bluff body used was a section of the cylinder with a cross-section corresponding to the centreplane of an Ahmed body with zero rear-slant angle. The dimensions were: height $H = 72$ mm, length $L = 262$ mm and width $W = 125$ mm. The domain is shown in Fig. 1 together with the definition of controlling parameters. A moving ground plane was used, translating at the same velocity as the inlet air, to mimic the effect of the body moving through a stationary fluid. The Reynolds number Re based on height H and U_∞ was 23,000.

A semi-structured mesh consisting of 8.6×10^6 elements, shown in cross-section in Fig. 2, was used to discretise the fluid volume. Dimensionless wall values for the ground proximity case are $\Delta x^+ \approx 10$–20 and $\Delta z^+ \approx 5$–50. With more of the fluid travelling over the body, the y^+ value reaches 10 over the upper leading edge, but is limited to $y^+ \approx 0.5 - 5$ over the rest of the body, with an average $y^+ = 2.5$. The mesh was kept identical to the away-from-ground model wherever possible, however this, of course, was not achievable in the ground region. In order to capture the ground proximity flow properly, a high mesh density was required in this region, increasing the final mesh to 8.6 million elements compared with 7.5 million elements for the away-from-ground case studied previously.

The large eddy simulations were run using the element-based finite-volume (FV) commercial code ANSYS CFX based on the standard Smagorinsky subgrid model. Quantities at the face between two control volumes are approximated from nodal values via shape functions for the non-advection terms.

For the advection term a blended scheme is used. This uses a weighted combination of a first and a second-order scheme; when the blend factor (β) is zero the scheme is first-order, and when it is set to one, the scheme is second-order accurate.

In this work, as with Krajnovic and Fernandes (2011), $\beta = 1$ is chosen, returning 2nd-order accuracy in space.

The diffusion and pressure gradient terms are also calculated from shape functions, and are 2nd-order.

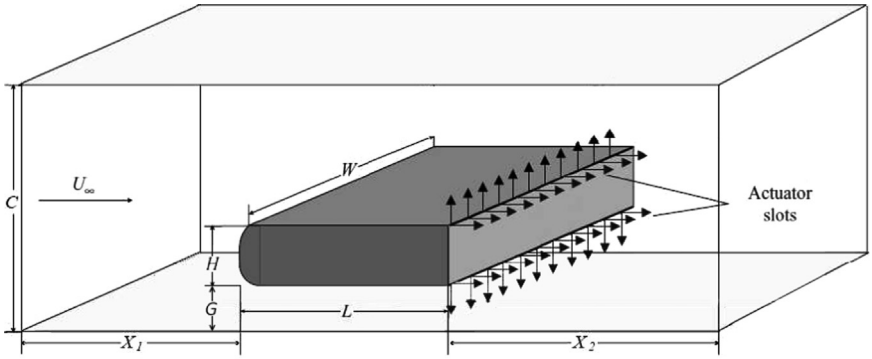

Fig. 1. Sketch of the 3D flow domain showing the problem setup, and key dimensions and parameters. The cylinder consists of an elongated rectangular cylinder but with rounded leading edges, consistent with the Ahmed body geometry cross-section. The ground clearance G is $0.2H$. The aspect ratio is $L/H = 3.64$. The computational domain dimensions are: $X_1 = 6.61H$, $X_2 = 24.47H$ and $C = 7.71H$. The domain extends into the third dimension a distance $W = 1.74H$. The blockage ratio is 13.0%. The origin (0, 0, 0) is at the centrepoint of the body's rear face. The positive x-direction is downstream parallel to U_∞, positive y-direction upwards parallel to C and positive z-direction into the page, parallel to W.

The 2nd-order (iterative) backward Euler-type scheme was used for temporal discretisation. A timestep of $\Delta t = 1 \times 10^{-4}$ s was used, giving a non-dimensional timestep $\Delta t^* = \Delta t\,(U_\infty/H)$ of 0.0058.

The Smagorinsky constant, C_s, was held constant at 0.1—a value leading to moderate damping of the subgrid eddy viscosity dissipation and often used for ground vehicle flows (Krajnovic, 2009).

These numerical methods and settings were unchanged from the study of Parkin et al. (2014) (the present authors), and the reader is directed there for further validation and discussions on the methodology, including effects of mesh resolution and computational settings. That paper also describes the application of Dynamic Mode Decomposition (DMD), which was used here to explore and characterise the dynamic modes in the wake.

While full velocity and pressure fields were recorded at every 50th timestep during the time integration, and the point-wise velocity was also recorded for every timestep at certain locations to monitor the higher-frequency fluctuations in the wake. The locations of these were at $1H$, $3H$ and $5H$ behind the rear, at heights of $\pm 0.5H$ from the mid-height of the body. Two shear layer monitors were also placed $0.21H$ behind the rear, at heights of $\pm 0.6H$.

The actuation signal was sinusoidal, and prescribed as a uniform velocity at the actuators (see Fig. 1) of $u_{act} = A\sin(\omega t)$, where A is the amplitude of oscillation and $\omega = 2\pi f_{act} = 2\pi St_{act}\,U_\infty/H$ defines the forcing frequency. This signal results in an outlet RMS velocity $u_{act,rms} = A/\sqrt{2}$. It is useful to quantify the level of forcing through a non-dimensional momentum coefficient expressed as

$$C_\mu = N_a \frac{S}{H}\frac{u_{act,rms}^2}{U_\infty^2}, \tag{1}$$

where N_a is the number of actuators (four for the dual slot actuation case shown in Fig. 1) and S/H is the ratio of the slot width (1 mm) to the height of the body (72 mm). This is just the ratio of the momentum flux through the slots to the notional momentum flux passing through the region occupied by the body. With the current setup, the actuators extend across the entire span, with two at the top rear edge facing vertically and horizontally, and another two at the bottom rear edge.

The total energy required to supply such a signal is relatively low: for the $Re_H = 23,000$ case, Pastoor et al. (2008) showed actuators at $c_\mu = 0.009$ require 0.094 W to operate, markedly lower than the power reduction from drag savings $\Delta P_D = U_\infty \Delta \overline{F}_x = 0.482$ W (where $\Delta \overline{F}_x$ is the time-averaged reduction in drag force) obtained for the away-from-ground case.

3. Results and discussion

As discussed in Section 1, the previous literature suggests a lower drag and less coherent vortex shedding would be expected with decreasing ground clearance. Indeed, these traits were observed here, along with many other noteworthy changes to the natural flow that are outlined in this section. Fig. 3 provides a depiction of the natural flow with the body at $X = 0.2H$ above the ground. It is characterised by separation over the upper leading edge, while staying attached underneath.

Note that all time-averaged fields and values quoted below were averaged from $t^* = 20$ to $t^* = 83$. Due to the high Reynolds number, the onset of turbulence after initiation of the simulation was almost instant, with fully turbulent characteristics such as vortex dislocation over the upper face and in the wake observed after the first two vortex pairs were shed. After this point, large scale fluctuations were minimal, and the mean quantities changed little with increasing time.

3.1. Natural flow statistics

The low-frequency meandering of the drag observed in the away-from-ground case is shown in Figs. 4 and 5 to be subdued in the ground proximity case, with the drag coefficient hovering around the mean value of 0.60 at all times. The higher frequency fluctuations related to the von Kármán instability, on the other hand, appear less consistent than the away-from-ground case. The PSD confirms this, with no single dominant frequency peak observed. The peak magnitude here is an order of magnitude lower than that observed for the corresponding frequency in the

Fig. 2. Cross-section of the mesh used for ground proximity study showing mesh distribution near the body. This 2D mesh was swept 70 elements into the Z-dimension (spanwise) to form the three-dimensional mesh.

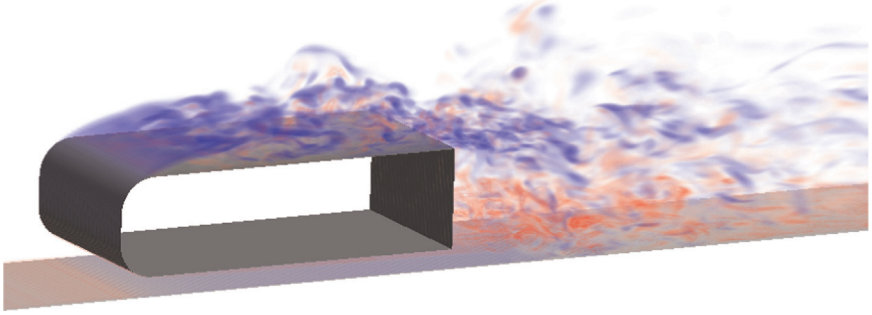

Fig. 3. A snapshot of a perspective view of the instantaneous spanwise vorticity for the natural flow over the body $0.2H$ above the ground. The blue–white–red colour map depicts spanwise vorticity from negative (clockwise) to positive (counter-clockwise) levels. (For interpretation of the references to color in this figure caption, the reader is referred to the web version of this article.)

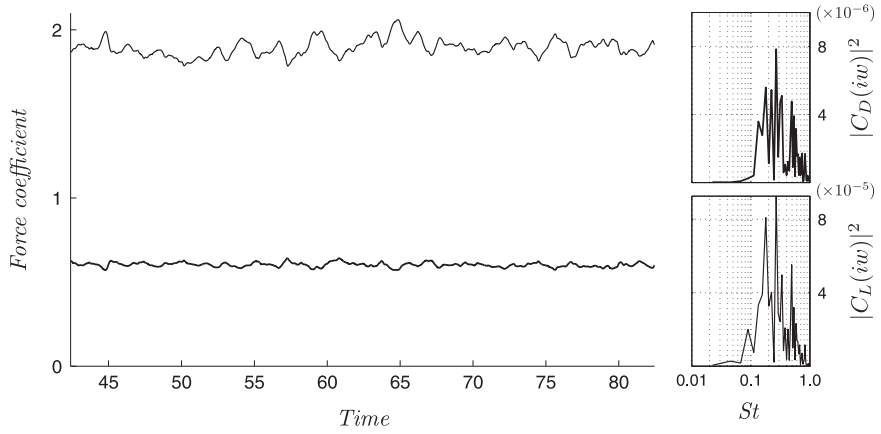

Fig. 4. Time history (time is displayed in non-dimensional time units, $t^* = tU_\infty/H$) of drag (thick line, lower) and lift (thin line, upper) signals for natural flow with ground clearance of 0.2*H*. The frequency spectrum for each signal is displayed on the right. The drag spectra amplitude (top right) is displayed at a scale one order of magnitude lower than the lift spectra amplitude (bottom right). The lift coefficient has a mean value of 1.86 – the reason for this high value is apparent in the time-averaged velocity and pressure contours discussed in Section 3.2.

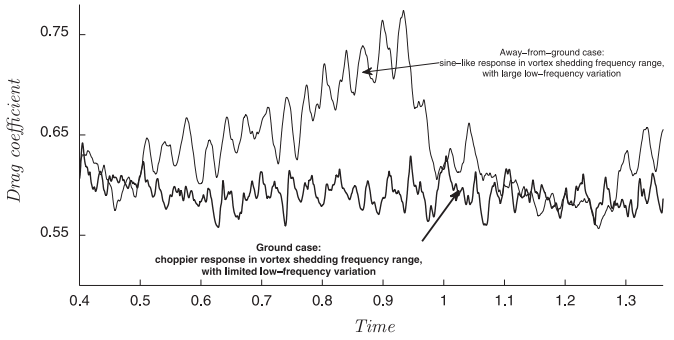

Fig. 5. Time history of drag signals for natural flow with ground clearance of 0.2*H* (thick line) and away-from-ground (thin line).

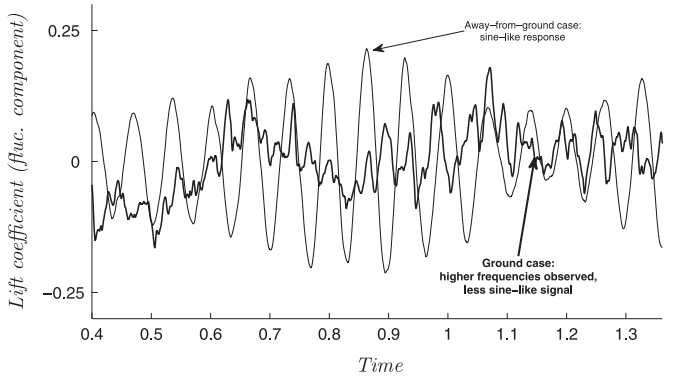

Fig. 6. Time history of fluctuating lift ($C_L - \overline{C_L}$, where $\overline{C_L}$ is the time-averaged lift coefficient) signals for natural flow with ground clearance of 0.2*H* (thick line) and away-from-ground (thin line).

away-from-ground case, while the areas under the peaks of each case are similar. The same differences occur in the lift signal, with irregular and higher frequency oscillations observed (Fig. 6). Combined, these features suggest that for the ground proximity case, the vortex shedding into the wake is less coherent than in the away-from-ground case (Table 1).

3.2. Natural time-averaged flow structure and topology

The time-averaged flow-field is significantly affected by the ground plane. Perhaps the most immediately obvious are the changes upstream of the rear face. The changed body configuration results in increased separation over the upper leading edge, with re-attachment occurring 2.26*H* downstream from the separation line, 41% greater than for the away-from-ground case. No separation occurs at the lower leading edge, with the flow beneath the body somewhat resembling a steady channel flow, complete with laminar boundary layer. In fact, to be more specific, this flow in this region represents classical *Couette* flow, where one surface is moving at the freestream velocity (here, the ground plane), while the other surface remains stationary (here, the lower body surface). That flow has a streamwise velocity profile, $U(y) = U_\infty \frac{y}{h} + \frac{1}{2\nu}\frac{dp}{dx}(y^2 - hy)$. When the pressure gradient is small, as is the case here, the first term is much larger than the second, which results in a near-constant shear stress throughout the region. While the mass flow rate in this "Couette" region (referred to as the channel region hereafter) remains constant as the rear edge is approached, the peak velocity slightly increases due to a growing boundary layer along the body's lower surface (Figs. 7–8).

The disparity at the front of the body leads to an asymmetric pressure profile, with the stagnation point occurring below the centrepoint of the nose. Furthermore, a large band of negative pressure appears in the separated region above the body. Together this results in a high average lift coefficient of 1.86.

3.3. The boundary layers

While the away-from-ground flow case features two identical (mirror-image) boundary layers, here there are three boundary layers, each with a unique profile (Fig. 9). The upper surface boundary layer is turbulent, and thicker than that observed in the away-from-ground case, due to the larger separated region over the upper front edge. The lower surface boundary layer is laminar and has a displacement thickness of 0.024*H* and momentum thickness 0.010*H*. The ground boundary layer is less typical—normally a surface moving at the freestream velocity features no boundary layer. However, here the fluid velocity reaches $1.15U_\infty$ at the lower rear edge (it is worth repeating here that U_∞ is the *corrected* freestream velocity) due to the slight pressure gradient between front and back, resulting in a difference in velocity between ground plane and the fluid in the centre of the channel. Thus, while Morton (1984) showed that no vorticity is generated at a surface moving in its own plane steadily, here a vorticity is generated due to the pressure gradient. This will be shown to influence the wake dynamics in Section 3.4.

Table 1
Natural flow statistics for away-from-ground case (first line) and ground proximity case (second line). $\overline{(\cdot)}$ represents time-averaged quantities.

Ground	$\overline{C}_D$	$C_{L,ave}$	$\overline{C}_{pb}$	St_D	$P\{D_{max}\}$	St_l	$P\{L_{max}\}$	t_{total} [a]
No	0.72	0 (0.29)[b]	−0.51	0.44	1.2×10^{-2}	0.22	2.8×10^{-5}	367 (5.38 s)
Yes	0.60	1.86	−0.38	0.27	7.8×10^{-6}	0.27	9.3×10^{-5}	83 (1.37 s)

[a] Note that the integration time for the ground proximity case corresponds to approximately 2.5 domain flow-through times.
[b] $C_{L,rms}$.

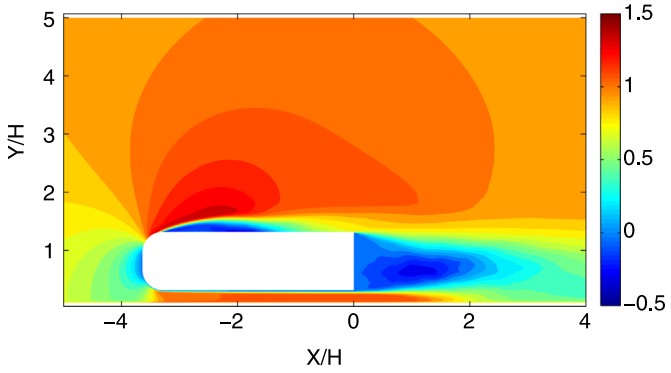

Fig. 7. Time-averaged u/U_∞ velocity along the centreplane.

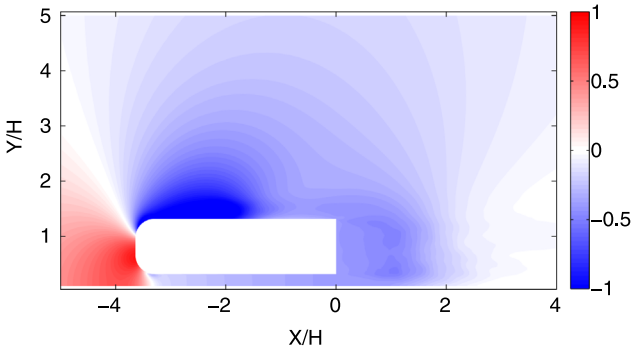

Fig. 8. Time-averaged pressure coefficient $\overline{C}_P$ contour through the centre plane.

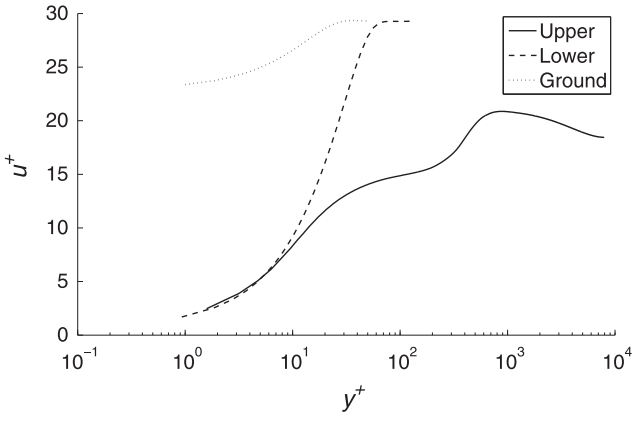

Fig. 9. Spanwise- and time-averaged boundary layer profile $X/H = -0.1$ (i.e. 0.1 upstream of the rear surface).

The upper-surface turbulent boundary layer has a momentum thickness of $0.5H$, and a displacement thickness of $0.58H$, both considerably larger than the boundary layer thickness of the away-from-ground case, which featured values of $0.019H$ and $0.025H$, respectively. This is primarily due to the greater separation length over the upper leading edge, which leaves less distance for a traditional boundary layer profile to reform further downstream.

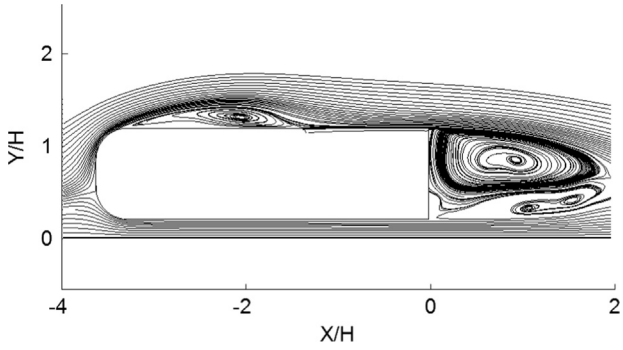

Fig. 10. Time-averaged velocity streamlines through the centre plane.

3.4. Natural Flow Wake

In the wake region the asymmetry of the time-averaged flow is less pronounced in the velocity and pressure contour plots. The dead-water region of the wake seems to occur halfway between the upper body surface and the ground plane, rather than halfway between the upper and lower body surfaces. Of further note is the perseverance of the flow from the lower channel into the wake region.

Time-averaged streamlines (Fig. 10) provide a clearer picture of the asymmetry in the near wake. The upper recirculation region dominates the wake, with the lower recirculation region narrower and far less pronounced. The centre of this lower recirculation region is further downstream than that of the upper ($1.34H$ compared to $0.95H$). The strong reverse flow region that results from these two opposing recirculation zones, and which normally occurs about the centreline of the wake, is pushed towards the ground plane in this case. This results in a region of minimal flow activity just downstream of the lower rear separation point, and upward travelling flow along the remainder of the rear face.

The Reynolds stress fields in the wake, shown in Fig. 11, are also noticeably different in the presence of ground. Both $\langle u'u' \rangle$ and $\langle v'v' \rangle$ feature a similar, though not identical, distribution, and are significantly less intense than for the away-from-ground case (Parkin et al., 2014). The $\langle u'v' \rangle$ component is at a similar level to the away-from-ground case, but does not feature the small oppositely-signed pocket regions near the base. The separatrix (i.e., the line representing the mean separation bubble which corresponds to the locations of the highest values of normal and shear stresses) extends $1.85H$ downstream from the frame, compared to $0.95H$ for the away-from-ground case.

Fig. 12 shows that, relative to the no ground plane case, the near wake features a higher pressure, with two low pressure regions vertically aligned a distance of $X \approx H$ behind the rear. This indicates that the upper and lower shear layers do not interact to

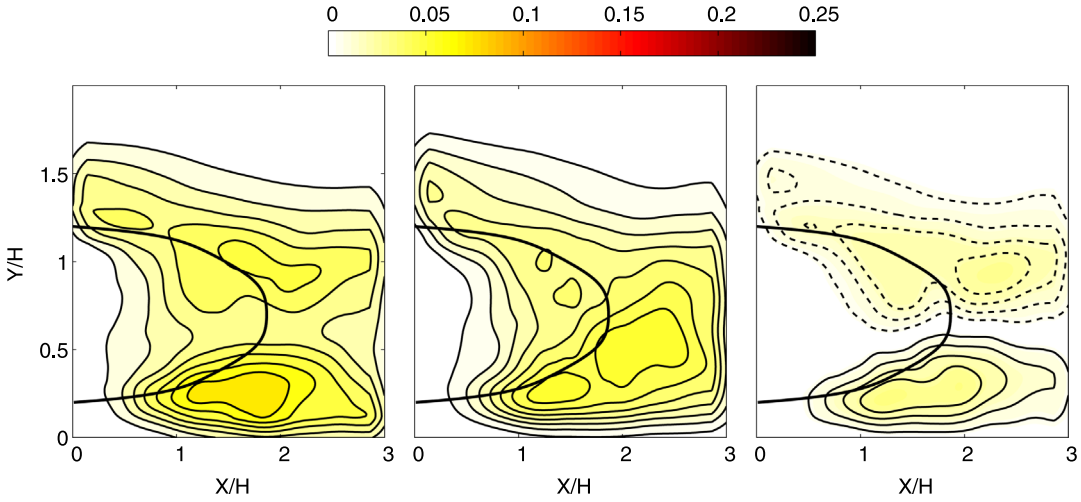

Fig. 11. Reynolds stress averages along the centreplane in the wake. From left to right: $\langle u'u' \rangle / U_\infty^2$, $\langle v'v' \rangle / U_\infty^2$, $\langle u'v' \rangle / U_\infty^2$. Dashed contour lines indicate negative magnitudes. The thick line indicates the separatrix (mean separation line).

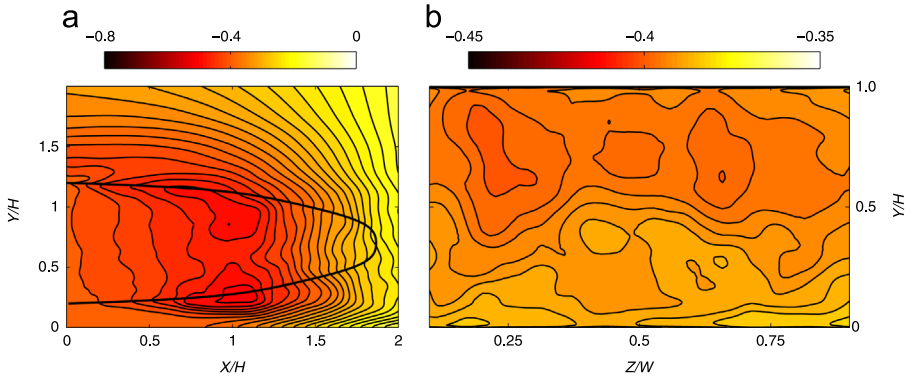

Fig. 12. (a) Time-averaged pressure coefficient $\overline{C_P}$ in the centreplane of the wake, and (b) on the rear base surface for $0.1 < Z/W < 0.9$. The thick line represents the separatrix.

form strong low-pressure wake vortices nearly as much as in the away-from-ground case. For the latter there is only one large low pressure region for the time-averaged flow (Parkin et al., 2014). On the rear surface, the pressure distribution is weakly asymmetric, with a slightly lower pressure observed over the upper half of the rear face (Fig. 12).

In conclusion, the main differences between the ground-proximity and the away-from-ground time-averaged wakes are a higher pressure throughout, lower Reynolds stresses, a longer wake length, and the introduction of asymmetry.

3.5. The von Kármán and Kelvin–Helmholtz instability modes

In addition to the time-averaged differences discussed above, an analysis of the transient results reveals that the dynamics in the wake are also significantly different from the away-from-ground case. The drag and lift signal analysis presented above suggested that the prevalence of vortex shedding in the wake is significantly diminished, and the velocity monitors add further evidence. No clear frequency peaks are observed in either the upper or lower positioned monitor points (Fig. 13). Other observations of the flow field confirm that no distinct vortex shedding is apparent.

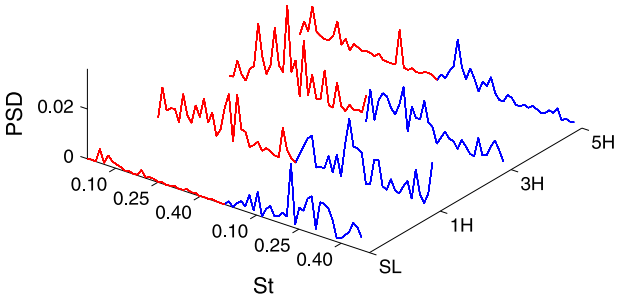

Fig. 13. Spectra of velocity monitors in the separating shear layer, 1H, 3H and 5H downstream of rear surface. The red line (left) represents the lower-wake monitors, while the blue line (right) represents the upper-wake monitors.

3.6. Natural flow dynamic mode decomposition

Dynamic mode decomposition confirms the absence of strong vortex shedding in the wake. The Ritz and mode magnitude plots, Fig. 14 (a) and (b), respectively, show no dominant dynamic mode (s) appear in the decomposition. The two highest magnitude modes are shown in Fig. 15, appear noisy with little coherent spatial structure, at least in the near wake. The modes appear slightly more structured further downstream. This is especially true for the second mode, where alternate-signed paired regions of vorticity at $X/H > 1$ are observed, and appear to be spaced apart at a regular interval. This, coupled with the lack of structure in the near-wake, reveals that the presence of the ground plane does

impose some regular dynamic behaviour on the flow, while limiting the vortex shedding.

However, it needs to be borne in mind that these dynamic modes are very weak, so that the mean mode superimposed with broadly unstructured turbulent structures is the overwhelming *modus operandi* of the natural flow. The mean mode, pictured in Fig. 14(c), is very strong, and also reveals some new insights to the flow. Two regions of opposite sign vorticity appear on the ground plane. These seem to affect the lower shear layer, which has a high vorticity at separation but does not extend as far downstream as the upper shear layer.

3.7. Actuated flow statistics

For the body in ground proximity, actuation was applied in the same manner as in Parkin et al. (2014), this time after 36 non-dimensional time units (0.58 seconds) of natural flow. This corresponds to approximately one flow through time. For the range of forcing frequencies and amplitudes tested, the actuation proved far less successful at reducing drag, with minimal changes observed in the mean drag for all actuation frequencies. Fig. 16 shows that, like in the away-from-ground case, the drag signal locks-on to the actuation signal almost immediately. In fact, the *amplitude* of the drag signal is even larger than that observed in the away-from-ground case. For the case shown, St_{act} = 0.22, the average drag signal amplitude is 0.21 for the former and 0.16 for the latter.

However, the lift signal responds in a completely different manner to that for the away-from-ground case, where it continued to oscillate at the natural Strouhal frequency but with less coherence. Here the lift signal locks-on to the actuation frequency for all cases, oscillating at large amplitudes, and the mean lift coefficient drops. A slight lag occurs, with the lift signal 15–35° behind the drag signal. This lag reduces as the actuation frequency increases.

The signals shown in Fig. 16 are broadly representative of all actuation frequencies examined. However, the amplitude of the drag signals grows slightly with increasing actuation frequency, while the amplitude of the lift signal decreases significantly. This is

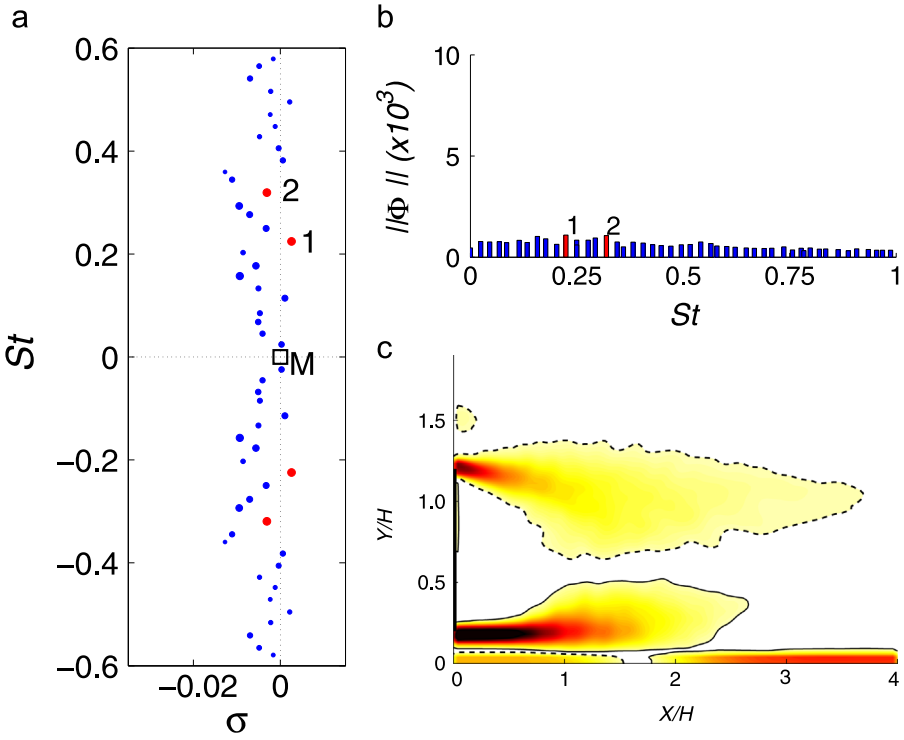

Fig. 14. Natural flow dynamic mode decomposition for the ground proximity case. (a) Spectrum showing the growth rate (σ) of each mode. The red dots are the most relevant modes, with the size of each dot showing its relative magnitude. The mean mode (M) is indicated with an open square. Modes 1 and 2 occur at St=0.22 and St=0.32 respectively, but are very weak. (b) The relative magnitude of each mode is plotted against frequency. (c) Vorticity contours for the mean mode. (For interpretation of the references to color in this figure caption, the reader is referred to the web version of this article.)

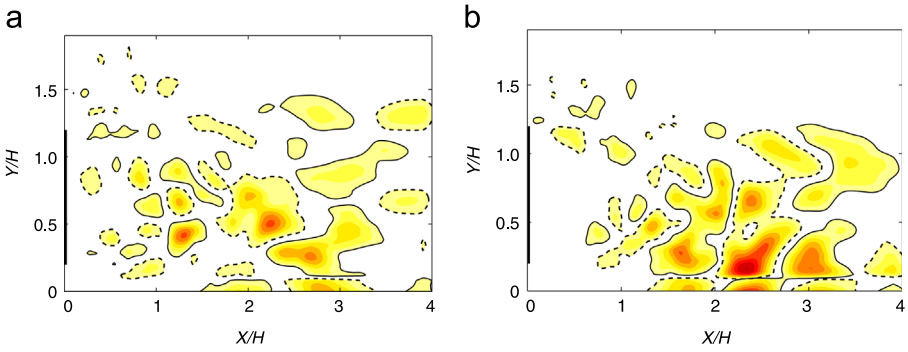

Fig. 15. (a) Vorticity contours of the highest magnitude dynamic mode, which occurs at a frequency of St=0.22. (b) Vorticity contours of the second highest magnitude dynamic mode, which occurs at a frequency of St=0.32.

represented in Fig. 17(b), which displays the spectral peaks of both signals. Once again, as was observed for the away-from-ground case, the lowest frequency case $St_{act} = 0.04$ shows small high frequency oscillations superimposed on the locked-on signals.

Despite the lock-on of both drag and lift signals, Fig. 17 (a) shows that the actuation has little impact on the mean drag value. The only case that appears to offer any drag reduction is the lowest frequency case, $St_{act} = 0.04$. However, the drag reduction obtained for this case is still well below that of the away-from-ground tests. This case shows a high natural frequency peak in the lift signal spectra, and a low actuation frequency peak in the drag spectra—in the away-from-ground case these features would correspond to the lowest drag reduction!

3.8. Effect of momentum coefficient

In an attempt to find a successful drag reduction case, the momentum coefficient was doubled to $C_\mu = 0.016$ for the case with $St_{act} = 0.35$. This proved to have the opposite of the desired effect, returning no change in the drag at all, compared to a 2.0% drag reduction at $C_\mu = 0.008$.

Finally, a case was tested with an asymmetric momentum coefficient set up: $C_\mu = 4 \times 10^{-3}$ for the upper slots combined, and $C_\mu = 8 \times 10^{-3}$ for the lower slots combined (resulting in a total $C_\mu = 0.12$). The idea behind this was to generate a strong perturbation in the lower shear layer so that this might result in larger more coherent vortices in the lower shear layer, in turn, so that they were closer in size to the upper layer vortices. This was indeed achieved through this configuration, however the result was a drag increase of 2.0%. As might be expected in retrospect, evening the size of the upper and lower vortices had no beneficial effect on the drag, as the natural case features minimal vortex shedding in the first place.

Thus, unfortunately, these simulations do not offer new insights into flow control for bodies in ground proximity.

3.9. Actuated time-averaged flow structure and topology

The time-averaged properties of the case $St_{act} = 0.195$, which produced results typical of all actuation cases, are analysed here to gain further insight into the actuated flow. The mean separation line indicates a shorter wake under actuation—opposite to the situation when the body was away from the ground. The Reynolds stresses, pictured in Fig. 18, are slightly larger than those observed in the natural case. The vertical velocity normal stress, $\langle v'v' \rangle$, experiences the largest increase, with a region of high energy fluctuations appearing at the centre of the mean separation line. The increased diffusion through these higher Reynolds stresses increases the curvature of the streamlines, leading to the a shorter recirculation zone.

The wake time-averaged pressure contours, Fig. 19, have a very similar topology to the natural case. However, here the minimum pressure regions are pushed closer to the base—for the natural case they were located at $X/H \simeq 1$, whilst here they are at located at $X/H \simeq 0.8$. Once again, this is the opposite of what was achieved for actuation away from ground, where the minimum pressure

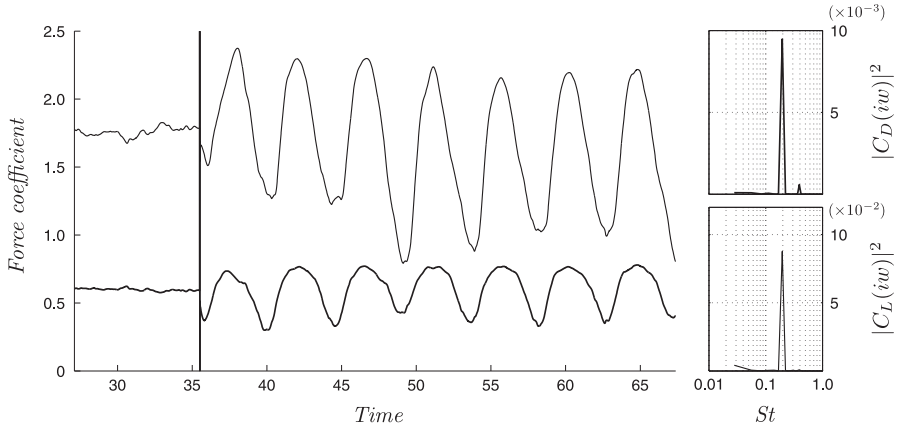

Fig. 16. Time history of drag (lower line) and lift (upper line) signals for $St_{act} = 0.195$. The frequency spectrum for each signal is displayed on the right. The drag spectra amplitude (top) is displayed at an order of magnitude lower than the lift spectra amplitude (bottom). Both signals return a distinct peak at the actuation frequency of 0.195. The discontinuity at $t=36$ corresponds to the switch from unforced to forced flow.

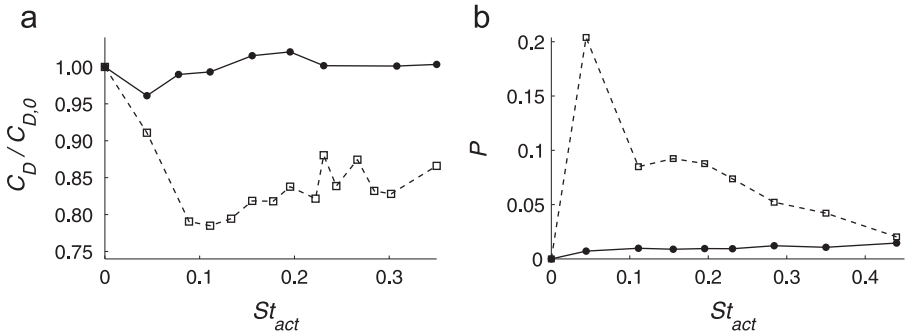

Fig. 17. (a) Numerical results for mean drag at different actuation frequencies. Thick line (filled dots) represents ground proximity with body $0.2H$ above ground plane; dashed line (open squares) represents away-from-ground case. (b) Magnitude of actuation frequency spectral peaks for drag signal ($P\{D_{act}\}$, closed circles) and for lift signal ($P\{L_{nat}\}$, open squares).

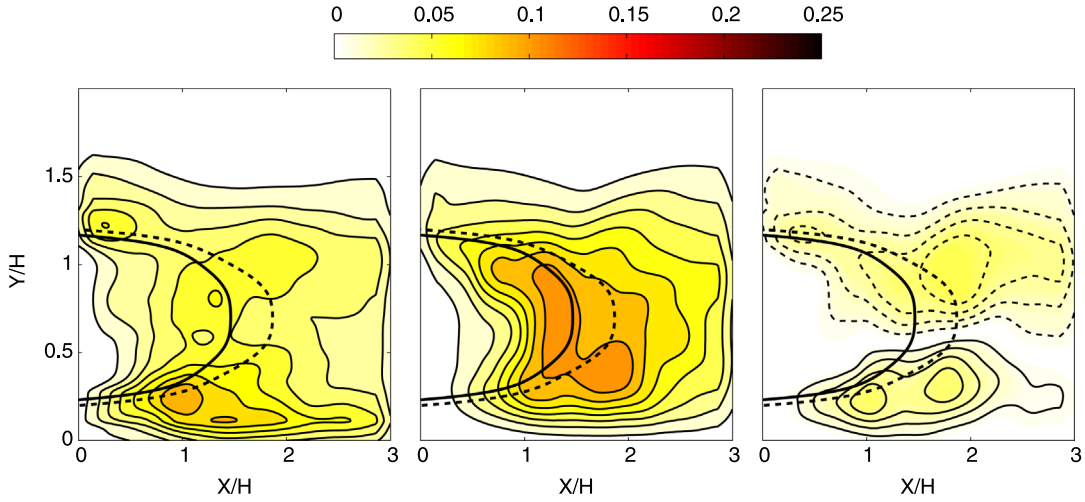

Fig. 18. Reynolds stress component fields in the centreplane for actuated flow at $St_{act} = 0.195$. From left to right: $\langle u'u' \rangle / U_\infty^2$, $\langle v'v' \rangle / U_\infty^2$, $\langle u'v' \rangle / U_\infty^2$. Dashed contour lines indicate negative magnitudes. The thick line indicates the separatrix (mean separation line); the dashed thick line indicates the separatrix for the unforced case.

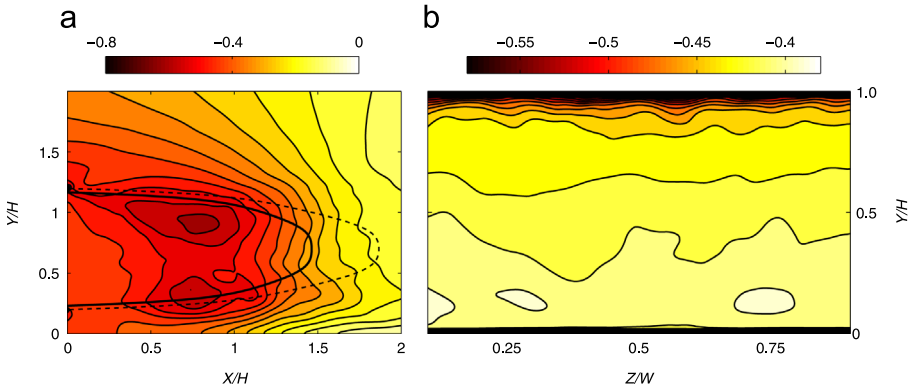

Fig. 19. Time-averaged pressure coefficient $\overline{C_P}$ on the centreplane through the wake (a), and (b) on the rear base surface for $0.1 < Z/W < 0.9$ (b) for $St_{act} = 0.195$. The thick line represents the separatrix; the dashed thick line indicates the separatrix of unforced case.

regions were pushed further downstream. Furthermore, the asymmetry of the base pressure profile in the natural ground case seems to be exaggerated by actuation. The lower half of the base has a time-averaged pressure similar to the natural case ($C_P \approx -0.39$), however, the upper half is markedly reduced, especially at the upper extremities, where C_P approaches -0.60.

3.10. Actuated flow dynamic behaviour

Velocity monitors in the wake reveal the lower shear layer is influenced more by actuation than is the upper separating shear layer. This is due to the greater turbulent fluctuations that occur in the upper shear layer, compared to the laminar lower shear layer. The spectra, therefore, return higher peaks for the bottom signals, as shown in Fig. 20.

The phase-averaged vorticity contours reveal the local maximum points in the drag and lift signals occur when the upper vortex is in the near wake, at $X/H \approx 0.7H$, while the local minimum points occur when the upper vortex has travelled further downstream to $X/H \approx 1.3$. The lower vortex shows a reduction in the vorticity between the maximum and minimum signal values, however, no change in position appears to be involved. The lower vortex generated by actuation appears to stagnate around $X/H = 1$, while only the upper convects further downstream (Fig. 21).

The dominance of the upper vortex reveals why the lift signal locks in to the actuation signal. In the away-from-ground case, the

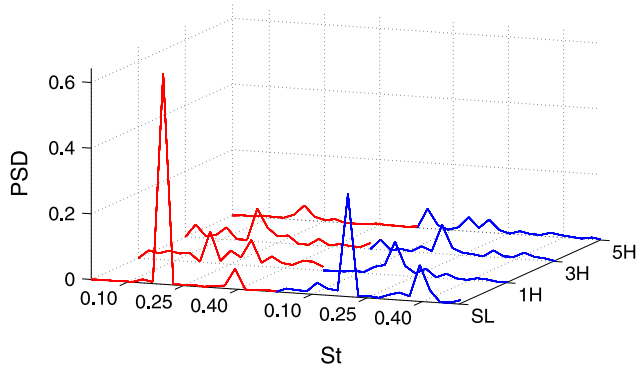

Fig. 20. Spectra of velocity monitors in the shear layer, $1H$, $3H$ and $5H$ downstream of the rear surface for $St_{act} = 0.195$. The red lines represent the lower-wake monitors, while the blue lines represent the upper-wake monitors. The dominant peaks occur at St_{act}. (For interpretation of the references to color in this figure caption, the reader is referred to the web version of this article.)

symmetric vortices are shed simultaneously, and there is therefore little net force imparted on the body in the vertical direction. Here, the motion of the upper vortex dictates the oscillations of the lift signal (and, of course, the drag signal). This causes very large oscillations in the lift signal; however, the oscillations are not large enough to create negative lift on the body at any point in time.

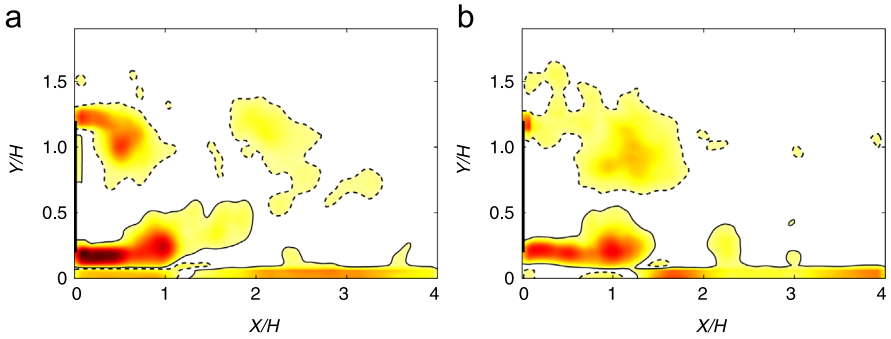

Fig. 21. Phase- and spanwise-averaged vorticity contours for St_{act} = 0.195 at drag signal (a) peaks and (b) troughs.

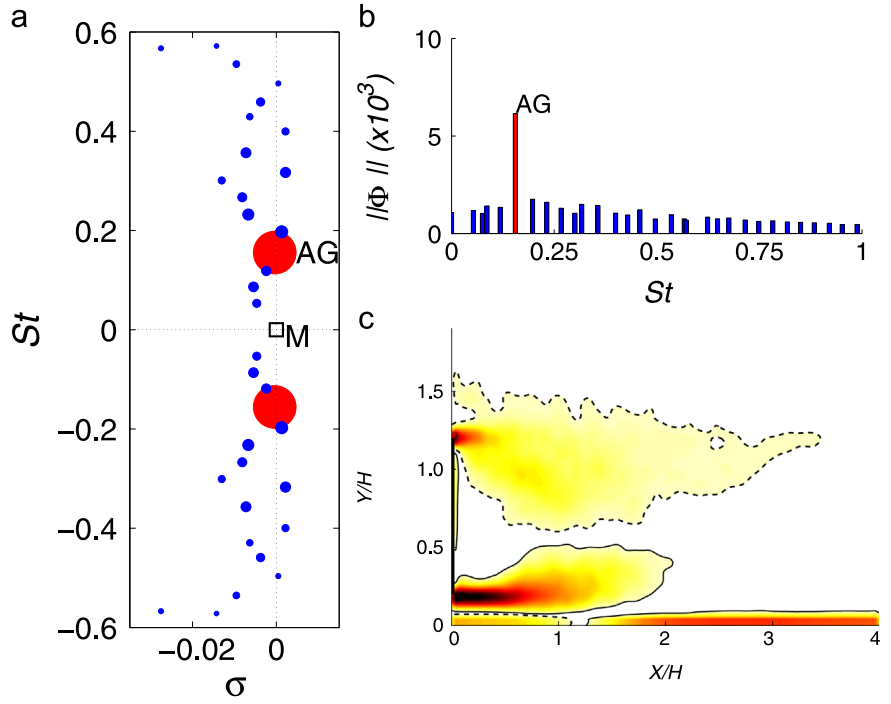

Fig. 22. Dynamic mode decomposition for St_{act} = 0.155. (a) Spectrum showing the growth rate (σ) of each mode. The red dots are the most relevant modes, with the size of each dot showing its relative magnitude. The mean mode (M) is indicated with an open square. Mode AG occurs at the actuation frequency, St_{act} = 0.155. (b) The relative magnitude of each mode is plotted against frequency. (c) Vorticity contours for the mean mode. (For interpretation of the references to color in this figure caption, the reader is referred to the web version of this article.)

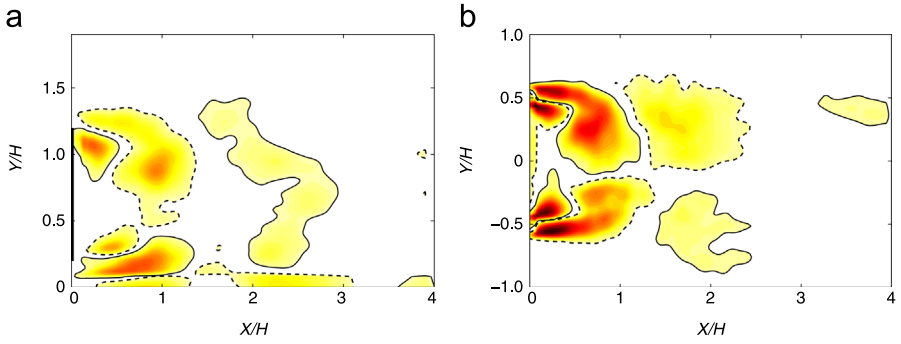

Fig. 23. Vorticity contours at St_{act} = 0.155 for the first unsteady Koopman mode in (a) the ground proximity case (mode AG), and (b) the away-from-ground case (mode A).

3.11. Actuated flow dynamic mode decomposition

For the natural ground-proximity case, dynamic mode decomposition revealed no clearly dominant dynamic modes in the wake. Applying actuation does, as expected, produce a dominant dynamic mode, as evident in the Ritz and mode magnitude plots of Fig. 22. Fig. 23 shows the mode shares similarities with mode A of the away-from-ground flow: namely, opposite-signed vortices are concurrently produced in the upper and lower shear layers. However, the vortices created here are not symmetric—the upper vortices are noticeably larger in size than the lower ones. Furthermore, an extra region of vorticity is observed on the ground plane. This complicates the evolution of the vortex pairs, resulting in a more intricate wake. Fig. 23 shows this evolution over half an

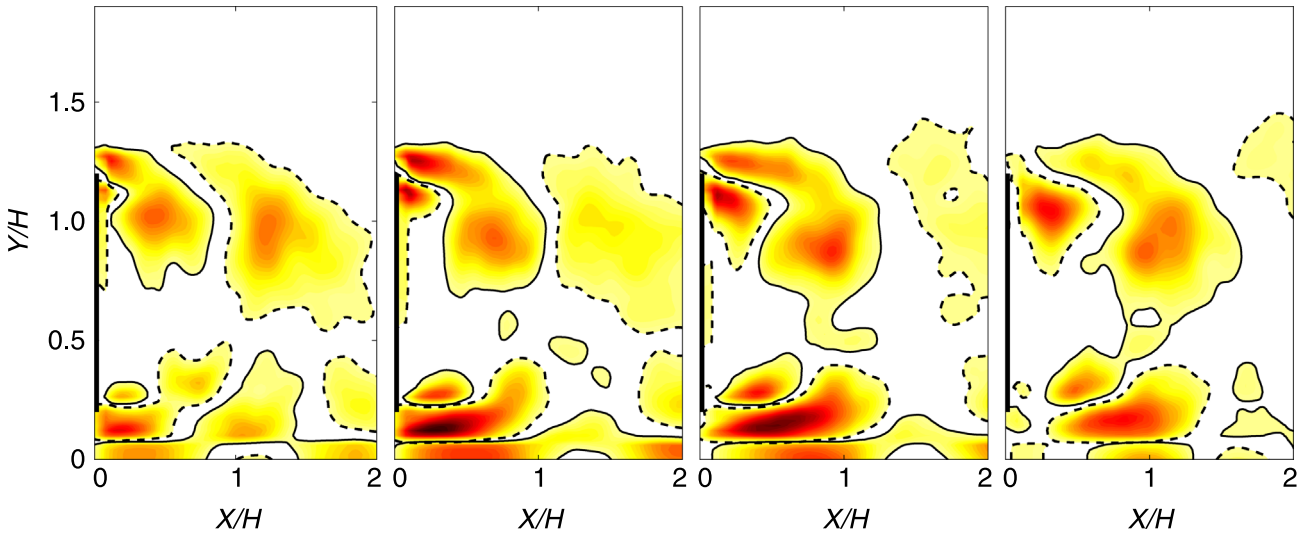

Fig. 24. St_{act} = 0.155: vorticity contours of half a cycle of first unsteady Koopman mode (mode *AG*). The second half of the cycle continues as above, but with opposite signed vorticity.

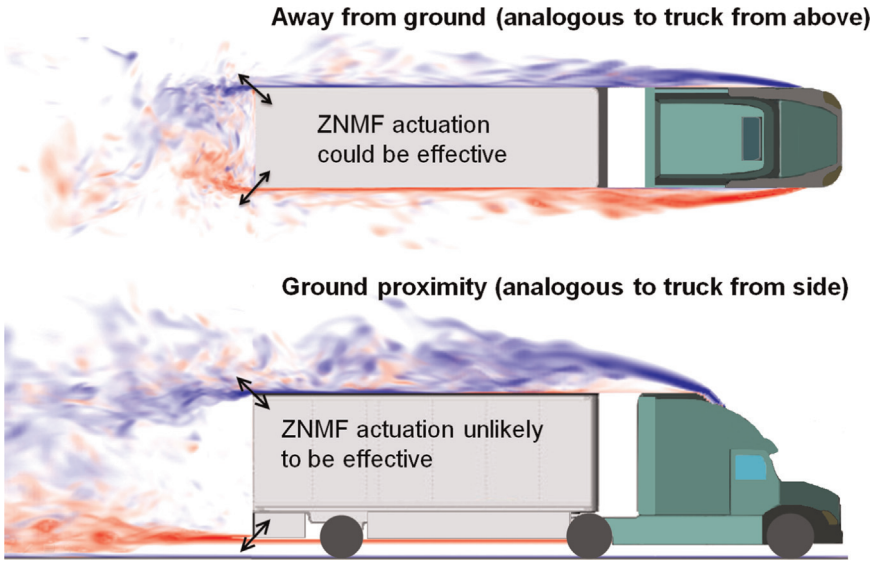

Fig. 25. Schematic of the possible speculative effect of Zero Net Mass Flux (ZNMF) actuation at the side and/or upper/lower rear edges of a truck-trailer. The blue/red colours indicate the superimposed flow structure from simulations presented in this paper and a previous paper (Parkin et al., 2014). The top image uses natural flow from the away-from-ground case, while the bottom image uses natural flow from the ground-proximity case. (For interpretation of the references to color in this figure caption, the reader is referred to the web version of this article.)

actuation cycle, allowing the mechanism to be analysed further. It can be seen that as the upper vortex grows, it moves towards the centre of the wake. This does not occur for the lower vortex, which grows in the streamwise direction rather than vertically towards the centre. The result is an uneven pair of vortices travelling downstream—the upper large vortex, resembling that created in the away-from-ground actuation, and the lower a thin, horizontally-aligned region above the ground. This structure is observed for all actuation cases, with the vortices becoming smaller at the higher actuation frequencies (Fig. 24).

The results suggest that the less coherent vortex shedding, which occurs for natural flow in the presence of a ground plane, is the major reason why this form of actuation, which attempts to mitigate vortex shedding, is ineffective. In the case of ground proximity, the upper and lower shear layers are no longer identical —the ground plane develops its own vorticity which interferes with the lower shear layer, while the upper shear layer is thicker and more turbulent due to the leading edge separation over the upper half of the body. This physical disparity reduces the propensity of the upper and lower shear layers to interact and roll-up leading to a coherent structured wake.

Wavelet analysis confirms the above findings: no dominant frequency is present in either the drag or lift signals for natural flow, while under actuation both the drag and lift signals lock on to the actuation frequency.

4. Conclusion

The results presented in this paper highlight a striking influence of ground proximity on the wake. The results suggest that a simple open-loop actuation strategy is unlikely to yield notable drag reductions for bluff bodies in the presence of a ground plane, e.g., those behind the upper and lower rear edges of a truck-trailer. It appears that the limited interaction of the shear layers, and their

asymmetry, renders the current technique of producing synchronous vortices to suppress von-Kármán shedding much less effective.

While this study aids understanding of bluff body aerodynamics and flow control, it cannot be directly applied to actual truck-trailers, which are, of course, three-dimensional bluff bodies, which operate at higher Reynolds numbers. They do, however, allow us to propose some new hypotheses on the suitability of this actuation technique on truck-trailers wake dynamics. From this study, together with the earlier one examining the flow without a ground plane, it appears that actuation is more likely to be successful if applied to the rear side edges of a trailer, where the opposite separating shear layers do not experience an unsymmetrical ground proximity effect, as opposed to the upper and lower rear edges, where the shear layers do. This idea is illustrated in Fig. 25.

However, recent work in fully characterising the dynamic wake behind a three-dimensional Ahmed-style flat-back body (Grandemange et al., 2013) suggests a more complex interaction of the four shear layers and corner vortices, which sheds some doubt on the validity of describing the wake as forming from two discrete pairs of shear layers as above, but the simplified picture may still represent a useful starting point. Further work in characterising the wake on three-dimensional flat-back bodies is clearly necessary. Of course, open-loop periodic actuation should also be attempted from the rear edges of these bodies, with testing on a full-scale truck-trailer the ultimate goal.

Acknowledgments

This research was undertaken with the assistance of a computing time grant obtained through the Merit Allocation Scheme of the National Computing Infrastructure (NCI) supported by the Australian Government. D.P. acknowledges financial support for a PhD scholarship through an Australian Research Council (ARC) Grant LP0991170.

References

Ahmed, S., Ramm, G., 1984. Some Salient Features of the Time Averaged Ground Vehicle wake. SAE Technical Paper No. 840300.

Grandemange, M., Gohlke, M., Cadot, O., 2013. Turbulent wake past a three-dimensional blunt body. Part 1. Global modes and bi-stability. J. Fluid Mech. 722, 51–84.

Kim, M., Geropp, D., 1998. Experimental investigation of the ground effect on the flow around some two-dimensional bluff bodies with moving-belt technique. J. Wind Eng. Ind. Aerodyn. 74-76, 511–519.

Krajnovic, S., 2009. Large eddy simulation of flows around ground vehicles and other bluff bodies. Phil. Trans. R. Soc. A 367, 2917–2930.

Krajnovic, S., Davidson, L., 2005. Influence of floor motions in wind tunnels on the aerodynamics of road vehicles. J. Wind Eng. Ind. Aerodyn. 93, 677–696.

Krajnovic, S., Fernandes, J., 2011. Numerical simulation of the flow around a simplified vehicle model with active flow control. Int. J. Heat Fluid Flow 32, 192–200.

Morton, B.R., 1984. The generation and decay of vorticity. Geophys. Astrophys. Fluid Dyn. 28, 277–308.

Parkin, D., Sheridan, J., Thompson, M.C., 2014. Numerical analysis of bluff body wakes under periodic open-loop control. J. Fluid Mech. 739, 94–123.

Pastoor, M., Henning, L., Noack, B.R., King, R., Tadmor, G., 2008. Feedback shear layer control for bluff body drag reduction. J. Fluid Mech. 608, 161–196.